corrosion and materials degradation

MDPI

Article

Stress Corrosion Cracking Susceptibility Prediction of 316L Austenitic Stainless Steel Based on Ensemble Learning

Luo-Wei Cao [1], Xue-Jia Yao [1], Qi-Heng Cai [2], Guang-Hai Li [1] and Xin-Yuan Lu [1,*]

[1] State Key Laboratory of Low-Carbon Thermal Power Generation Technology and Equipments, China Special Equipment Inspection & Research Institute, Beijing 100029, China; lwcao_1794@126.com (L.-W.C.); yao_xuejia@126.com (X.-J.Y.); liguanghai@csei.org.cn (G.-H.L.)
[2] Zhejiang Academy of Special Equipment Science, Hangzhou 310018, China; caiqiheng1997@126.com
* Correspondence: luxinyuan66@126.com; Tel.: +86-010-5906-8302

Abstract

Stress corrosion cracking (SCC) threatens the service integrity of 316L stainless steel in aggressive aqueous environments. With 316L stainless steel as the target application, this study evaluates a particle swarm optimization–extreme gradient boosting (PSO-XGBoost) framework for predicting SCC occurrence using a constructed dataset of 71 records. Temperature, chloride concentration, and oxygen concentration are used as model inputs. Predictive performance is assessed using stratified four-fold cross-validation, with hyperparameter selection conducted within the training partitions. Decision trees, random forests, and fixed-parameter XGBoost are included for comparison. PSO increases the pooled out-of-fold Accuracy of XGBoost from 77.46% to 80.28%. Classification-threshold adjustment further increases Accuracy to 81.69%, with a Matthews correlation coefficient of 0.6348. Environmental response maps are constructed at 260 °C and 340 °C using the refitted model. The high-risk region is larger at 340 °C, and this ordering persists across the 25 combinations of zoning boundaries examined. The results demonstrate improved classification performance on the constructed dataset and provide a quantitative basis for comparing relative SCC response regions under different environmental conditions.

Keywords: 316L stainless steel; stress corrosion cracking; XGBoost; particle swarm optimization; cross-validation

1. Introduction

Austenitic stainless steels are widely used in light-water reactors because of their corrosion resistance. Stress corrosion cracking (SCC) occurs when a susceptible material is subjected to tensile stress in a specific corrosive environment [1]. In high-temperature chloride-containing water, temperature, chloride concentration, and oxygen concentration can describe the environmental conditions and serve as inputs for predicting SCC occurrence.

Mechanistic models predict SCC growth by describing deformation and environmental reactions near the crack tip [2]. Film-rupture and slip-dissolution models link slip-induced surface-film rupture with subsequent dissolution to describe sustained crack advance [3,4]. The Shoji models use crack-tip strain rate to characterize local deformation and incorporate oxidation kinetics into the description of crack growth [5–7]. Steady-state crack-growth fields in strain-hardening materials provide a basis for the associated crack-tip mechanical analysis [8]. Coupled environment fracture models account for interactions between

Check for updates

Academic Editor: Raman Singh

Received: 7 September 2026
Revised: 16 November 2026
Accepted: 22 November 2026
Published: 26 November 2026

Copyright: © 2026 by the authors. Licensee MDPI, Basel, Switzerland. This article is an open access article distributed under the terms and conditions of the Creative Commons Attribution (CC BY) license.

electrochemical processes inside and outside the crack and examine their effects on crack propagation [9–11].

Machine learning has been used to establish relationships between material characteristics and SCC behavior. Zhou et al. developed a model for predicting intergranular cracking in stainless steels exposed to high-temperature water using grain-boundary descriptors [12]. To investigate environmental effects, Smets and Bogaerts applied artificial neural networks to cracking susceptibility in austenitic stainless steels exposed to chloride-containing water [13,14]. Smets and Bogaerts subsequently combined a neural network with an expert system to assess SCC susceptibility in high-temperature reactor water [15]. Lu subsequently used neural networks to predict steady-state crack-growth rates in sensitized Type 304 stainless steel [16]. Shi et al. investigated crack-growth rates in Type 304 stainless steel and Alloy 600, applying neural networks to SCC propagation under different material conditions [17,18].

Among ensemble approaches, XGBoost has been combined with SHAP analysis to investigate how alloy composition and applied stress relate to SCC resistance [19]. Falaakh and Bahn used CatBoost to predict crack-growth rates in stainless steels under light-water-reactor conditions [1]. They further calibrated the predictive uncertainty and used model explanations to examine the effects of the input variables.

Using MatFold, Witman and Schindler compared random partitions with validation grouped by material characteristics and found that the estimated error of a modeling approach changed with the partitioning strategy [20]. Li et al. found that some nominally out-of-distribution test sets remained within the representational coverage of the training data; predictions were weaker in poorly covered regions, where expanding the training set provided limited improvement [21].

With 316L stainless steel as the target application, this study evaluates a PSO-XGBoost framework for SCC occurrence prediction using temperature, chloride concentration, and oxygen concentration. A 71-record dataset is analyzed using fixed outer cross-validation partitions, with parameter selection performed within the training partitions. Out-of-fold predictions are compared with those from DT, RF, and fixed-parameter XGBoost. PSO selects the number of trees and maximum tree depth, and classification thresholds are subsequently determined from training-partition validation predictions. The fitted model is then used to construct fixed-temperature environmental response maps. Perturbation of the zoning boundaries quantifies how the resulting relative-risk regions depend on the selected output levels.

2. Methods

2.1. Decision Tree

A decision tree recursively partitions samples using feature thresholds until they reach terminal leaves. Predictions are obtained from the class distribution within each leaf. Figure 1 illustrates the structure of a binary classification tree.

The classification and regression tree (CART) algorithm is used to construct the decision tree. Node impurity is measured using the Gini index:

$$G = 1 - \sum_{k=1}^{K} p_k^2 \quad (1)$$

where K is the number of classes and p_k is the proportion of class k within the node. For binary classification, the expression reduces to:

$$G = 2p(1 - p) \quad (2)$$

where p is the positive-class proportion. CART compares the weighted Gini impurity of the child nodes to determine the splitting feature and threshold.

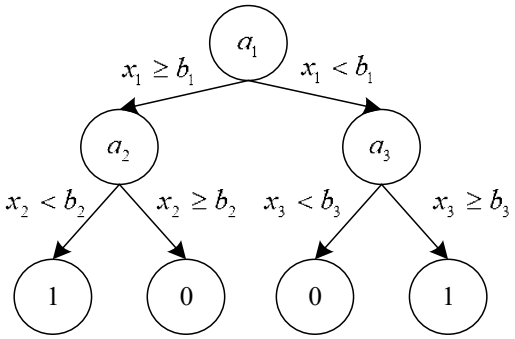

Figure 1. Schematic structure of a binary classification tree.

2.2. Ensemble Learning

Ensemble learning combines the outputs of multiple base learners. Bagging trains learners on bootstrap samples of the training data and aggregates their predictions [22]. Boosting trains learners sequentially, using information from the current model's loss to update the predictions.

Random forest (RF) combines multiple decision trees for prediction [23]. Each tree is trained on a bootstrap sample, and candidate splits are evaluated using a randomly selected subset of features. Its structure is shown in Figure 2.

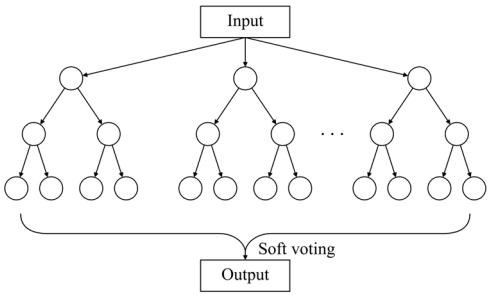

Figure 2. Construction and prediction process of random forest.

The RF implementation used in this study averages the positive-class probabilities from the trees and applies a classification threshold to obtain the predicted class.

XGBoost updates the model score by adding regression trees sequentially [24]. At each round, a new tree is learned using information from the current loss, and its contribution is scaled by the learning rate. For an ensemble containing m trees, the model score is:

$$F_m(x) = F_0(x) + \eta \sum_{k=1}^{m} f_k(x) \tag{3}$$

where F_0 is the initial score, f_k is the output of the k-th tree, and η is the learning rate. For the binary classification task considered here, the model score is converted to the SCC-positive-class probability using the sigmoid function:

$$p_i = \frac{1}{1 + \exp[-F_m(x_i)]} \tag{4}$$

Given a classification threshold τ, the predicted class is:

$$\hat{y}_i = \psi(F_m(x_i)) \{ \begin{matrix} 1, p_i \geq \tau \\ 0, p_i \tau \end{matrix} \tag{5}$$

Class 1 denotes SCC occurrence, and class 0 denotes no SCC. The mapping ψ applies the sigmoid transformation followed by the classification threshold.

XGBoost constructs new trees using first- and second-order loss derivatives. For binary logistic loss, the derivatives evaluated at the previous-round model score are:

$$g_i^{(t)} = p_i^{(t-1)} - y_i$$
$$h_i^{(t)} = p_i^{(t-1)}(1 - p_i^{(t-1)}) \quad (6)$$

where y_i is the observed class and $p_i^{(t-1)}$ is the positive-class probability from the previous round. The quantities $g_i^{(t)}$ and $h_i^{(t)}$ are the first- and second-order derivatives of the loss with respect to the model score, respectively.

Before learning-rate shrinkage, the second-order approximate objective for the candidate tree at round t is:

$$\tilde{L}^{(t)} = \sum_{i=1}^{n} [g_i^{(t)} f_t(x_i) + 0.5 h_i^{(t)} f_t^2(x_i)] + \Omega(f_t) \quad (7)$$

where n is the number of samples in the current training set. Tree complexity is controlled by the regularization term:

$$\Omega(f_t) = \gamma J_t + 0.5\lambda \sum_{j=1}^{J_t} \omega_{tj}^2 \quad (8)$$

Here, J_t is the number of leaves in tree t, and w_{tj} is the output weight of leaf j. The parameter γ penalizes additional leaves, while λ constrains the magnitude of the leaf weights.

Figure 3 illustrates the sequential updates from the initial score to the final classification output. Loss derivatives are recalculated from the current model at each round to learn the next tree.

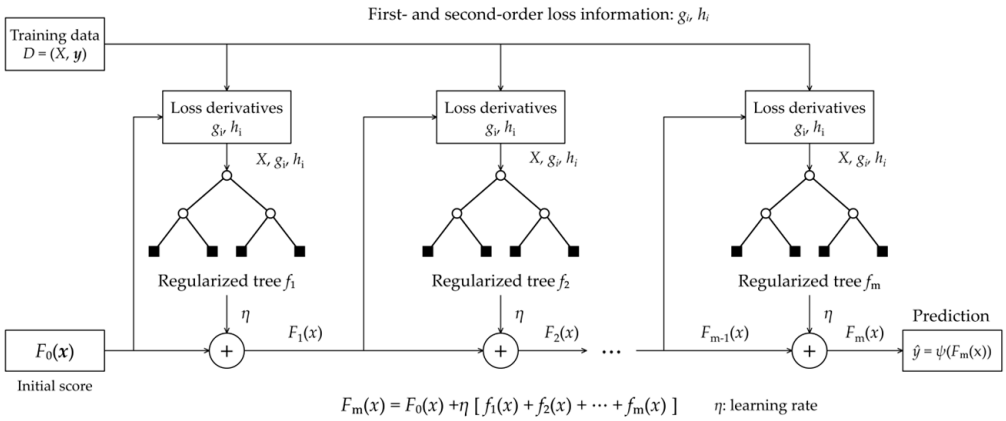

Figure 3. Sequential tree addition in XGBoost.

2.3. Particle Swarm Optimization

Particle swarm optimization (PSO) updates candidate solutions by sharing search information among particles [25]. Each particle retains its best visited position and adjusts its motion using the best position found by the swarm. The velocity and position of particle r in dimension j are updated as follows:

$$v_{rj}^{(t+1)} = \omega v_{rj}^{(t)} + c_1 r_1 (p_{rj}^{(t)} - z_{rj}^{(t)}) + c_2 r_2 (q_j^{(t)} - z_{rj}^{(t)}) \quad (9)$$

$$z_{rj}^{(t+1)} = z_{rj}^{(t)} + v_{rj}^{(t+1)} \quad (10)$$

Here, z and v denote particle position and velocity, respectively. The personal best position is p, and the swarm's historical best position is q. The inertia weight is ω, and c_1 and c_2 are acceleration coefficients. The random numbers r_1 and r_2 are drawn from $[0, 1]$ independently for each particle and dimension at every update.

The two particle-position components represent the number of trees and maximum tree depth of XGBoost. Positions are rounded to integers and constrained to the prescribed search ranges before evaluation. Each candidate is assessed by cross-validation within the training partition, and Accuracy and MCC are calculated from the pooled validation predictions.

A classification threshold of 0.50 is used during optimization. Candidates with higher Accuracy are preferred. Ties in Accuracy are resolved using higher MCC, and the existing best position is retained when both metrics are equal.

The swarm contains 80 particles and undergoes 300 updates after the initial evaluation. The inertia weight is 0.8, and both acceleration coefficients are 2. The search range is 1–150 for the number of trees and 1–30 for maximum tree depth. Initial velocities are sampled within ±10% of the search span in each dimension, and updated velocities are limited to ±50% of that span. The fixed-parameter XGBoost configuration is included in the initial swarm.

Figure 4 presents the PSO-XGBoost parameter optimization process. Candidate particles are converted to model parameters and evaluated through inner validation. The resulting fitness values are used to update the best positions and particle motion.

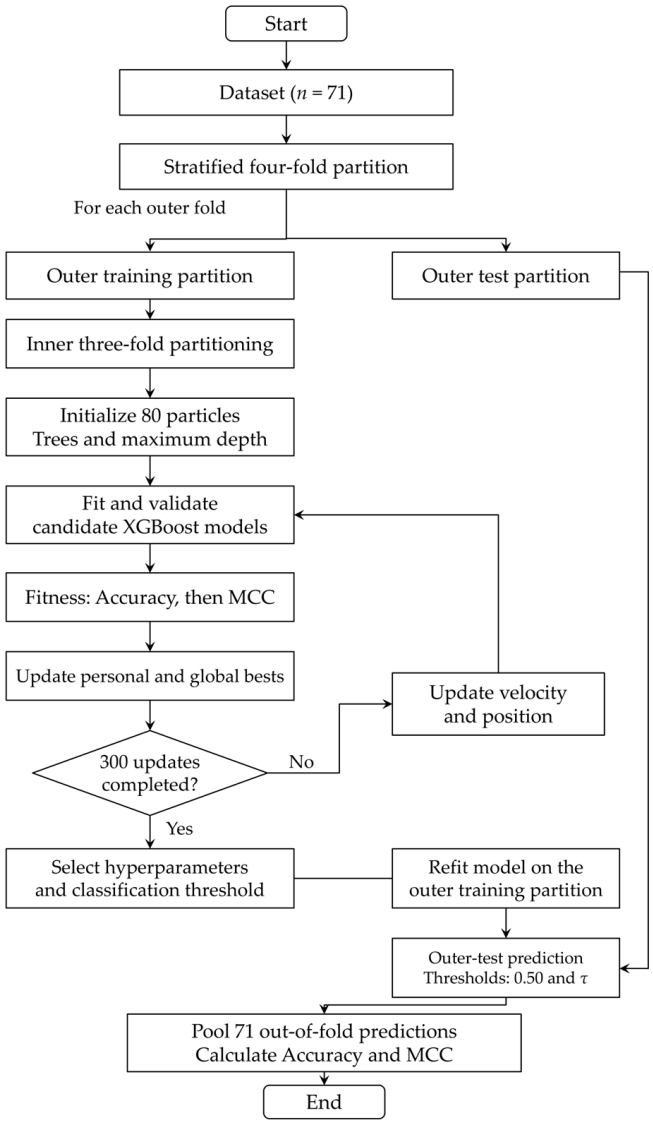

Figure 4. PSO-XGBoost parameter optimization using inner-validation evaluation.

3. Data and Validation Methods

3.1. Data Preparation

Temperature, chloride concentration, and oxygen concentration describe the environmental conditions associated with SCC in high-temperature water [26]. The dataset contains 71 records. Input ranges and SCC class encoding are summarized in Table 1.

Table 1. Input ranges and SCC class encoding.

Variable	Unit	Range or Encoding
Temperature	°C	241–350
Chloride concentration	mg/L	0.001–2631.42
Oxygen concentration	mg/L	0.01–1080.96
SCC class	-	1: SCC; 0: no SCC

The dataset contains 33 SCC-positive and 38 SCC-negative records. The two concentration variables are log10-transformed relative to a reference concentration of 1 mg/L and used together with temperature as model inputs. Min–max normalization parameters are fitted on the current training partition and applied to the corresponding validation or test partition.

3.2. Cross-Validation and Parameter Selection

The analyses were performed in Python 3.12.14. The DT and RF models were implemented using scikit-learn 1.9.1, and the XGBoost models were implemented using XGBoost 3.4.1.

A fixed stratified four-fold cross-validation partition is used, with 18, 18, 18, and 17 records in the outer-test folds. Parameters are selected through three-fold inner validation within each outer training partition. The selected model is then refit on that partition and used to predict the corresponding outer-test records [27]. All models use the same partitions, and each record receives one out-of-fold prediction.

DT and RF use random search on the same inner partitions. Their candidate counts are capped at the number of distinct parameter combinations evaluated by PSO in the corresponding fold. Principal settings are summarized in Table 2. Candidates are selected using the Accuracy and MCC rule described in Section 2.3.

Table 2. Model parameters and search settings.

Model	Selection Method	Parameter Range or Value	Principal Fixed Settings
DT	Random search	Max. depth: 1–30; min. leaf size: 1–30	Gini criterion
RF	Random search	Trees: 1–150; max. depth: 1–30	Features per split: 1
Fixed-parameter XGBoost	Fixed	Trees: 100; max. depth: 6	Learning rate: 0.3
PSO-XGBoost	PSO	Trees: 1–150; max. depth: 1–30	Learning rate: 0.3

Models are compared at a classification threshold of 0.50. For PSO-XGBoost, the threshold is also selected from 0.30 to 0.70 in steps of 0.01 by maximizing pooled inner-validation Accuracy, with higher MCC resolving ties, and applied to the corresponding outer-test predictions.

3.3. Performance Evaluation

Accuracy is the proportion of correctly classified records. MCC evaluates classification performance using the confusion matrix:

$$MCC = \frac{TP \cdot TN - FP \cdot FN}{\sqrt{(TP + FP)(TP + FN)(TN + FP)(TN + FN)}} \quad (11)$$

Here, TP and TN are the numbers of correctly classified positive and negative records, respectively, while FP and FN are false positives and false negatives.

Overall metrics are calculated from the 71 pooled out-of-fold predictions, with fold-specific scores reported separately. Models are compared using paired predictions for the same records. ROC-AUC is calculated from continuous out-of-fold probabilities as a supplementary measure of class-ranking performance.

3.4. Sensitivity Analysis

A response model is selected by three-fold validation and refitted on all 71 records to construct environmental contours at 260 and 340 °C. A 501 × 501 grid is constructed in log10 concentration coordinates, covering 0.001–3000 mg/L chloride and 0.01–1200 mg/L oxygen.

Outputs below 0.35, from 0.35 to below 0.60, and at least 0.60 define low, medium, and high relative-risk zones, respectively. Displayed curves use Gaussian smoothing with a standard deviation of 0.10 log10 concentration units. Plotted records are restricted to temperatures within 15 °C of the displayed slice. Raw and smoothed outputs are evaluated separately.

Using 0.35/0.60 as the baseline, each boundary is varied within ±0.05 in increments of 0.05, producing nine combinations. Extending the variation to ±0.10 produces 25 combinations. Category coverage is calculated by trapezoidal integration over the log10 concentration domain, and spatial agreement is the area fraction retaining its baseline category. High-risk coverage is compared between the two temperatures, and changes in risk assignments are calculated for the 71 out-of-fold records.

4. Results and Discussion

4.1. Model Comparison and PSO

Table 3 summarizes pooled out-of-fold performance using a common classification threshold of 0.50. PSO-XGBoost achieves the highest Accuracy and MCC, reaching 80.28% and 0.6044, respectively. Compared with fixed-parameter XGBoost, the number of correct predictions increases from 55 to 57, corresponding to an Accuracy improvement of 2.82 percentage points.

Table 3. Pooled out-of-fold performance at a common classification threshold.

Model	Accuracy (%)	MCC	ROC-AUC
DT	76.06	0.5235	0.7767
RF	78.87	0.5770	0.8581
XGBoost	77.46	0.5470	0.8589
PSO-XGBoost	80.28	0.6044	0.8210

Figure 5 shows selected early particle positions in the first outer training fold. The initial swarm covers a broad parameter region. Across the displayed stages, particles become increasingly concentrated toward fewer trees and shallower depths.

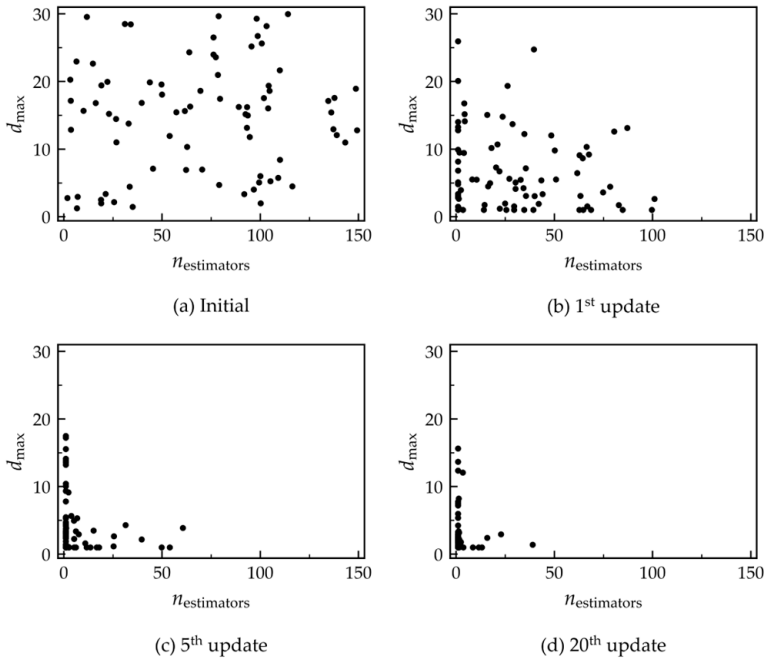

Figure 5. Selected early particle positions in the first outer training fold: (**a**) initialization; (**b**) update 1; (**c**) update 5; and (**d**) update 20.

Figure 6 shows the best-so-far inner-validation performance over the first 10 updates in the first outer fold. Accuracy increases from 75.47% to 77.36%, while MCC increases from 0.5030 to 0.5430. The improvement occurs at update 2, and subsequent search updates do not produce a higher inner-validation score.

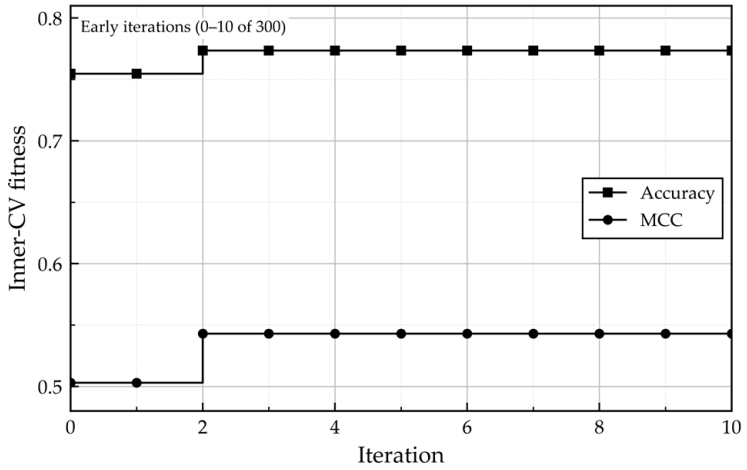

Figure 6. PSO convergence curves.

Figure 7 compares fixed-parameter XGBoost and PSO-XGBoost across the four outer-test folds. PSO-XGBoost achieves higher Accuracy and MCC in Folds 1 and 2, matches the baseline in Fold 3, and performs less well in Fold 4. The improvement in pooled performance therefore reflects the combined gains and losses across the test folds.

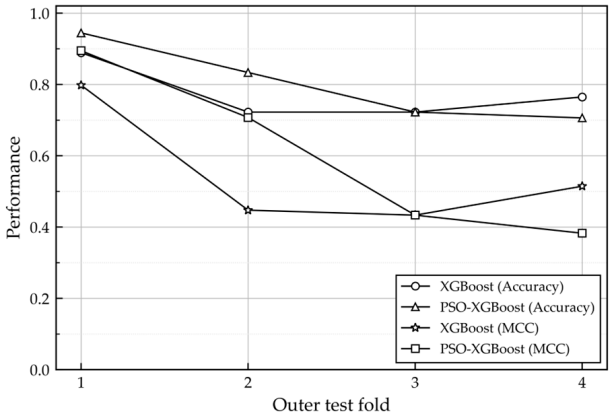

Figure 7. Accuracy and MCC of fixed-parameter XGBoost and PSO-XGBoost across four outer-test folds at a classification threshold of 0.50.

4.2. Environmental Response and Relative-Risk Zoning

Figures 8 and 9 present environmental response contours at 260 and 340 °C. Over the same concentration domain, high-risk coverage in the raw output grid increases from 32.33% at 260 °C to 58.46% at 340 °C, a difference of 26.12 percentage points. The higher-temperature slice contains a larger high-risk region.

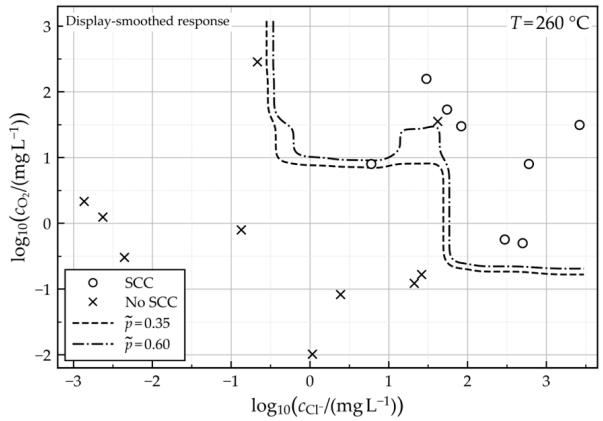

Figure 8. Display-smoothed relative SCC risk contours at 260 °C. Dashed and dash-dot lines indicate output levels of 0.35 and 0.60, respectively. Circles and crosses denote SCC-positive and SCC-negative records within 245–275 °C.

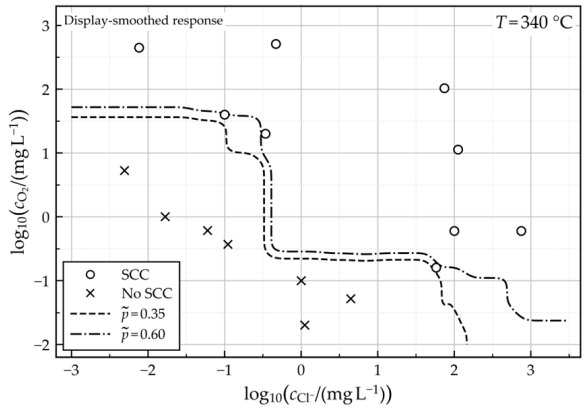

Figure 9. Display-smoothed relative SCC risk contours at 340 °C. Symbols follow Figure 8; plotted records are selected from 325 to 355 °C.

Table 4 summarizes the minimum spatial agreement under threshold perturbations. Across all 25 scenarios, high-risk coverage at 340 °C remains greater than at 260 °C, with differences of 23.39–26.62 percentage points in the raw grids.

Table 4. Minimum spatial agreement with baseline zoning under threshold perturbations (%).

Temperature (°C)	Output	±0.05	±0.10
260	Raw	98.48	97.71
260	Smoothed	98.38	97.22
340	Raw	97.57	94.47
340	Smoothed	97.00	92.98

The medium-risk band varies more substantially. At 340 °C, its baseline coverage in the raw grid is 4.96%, compared with a range of 0.85–10.07% under the extended perturbations. Among the 71 out-of-fold records, up to 19 change categories across the nine primary scenarios, increasing to 23 across the 25 extended scenarios.

Under the baseline zoning, SCC-label proportions are 21.43%, 48.00%, and 83.33% in the low-, medium-, and high-risk groups, respectively. Three extended scenarios reverse the ordering of the label proportions in the low- and medium-risk groups. The medium-risk band and record-level assignments are therefore more sensitive to the boundaries than the overall coverage difference between the two temperature slices.

4.3. Classification-Threshold Adjustment

Inner validation selects a classification threshold of 0.50 in the first three folds and 0.68 in Fold 4. Applying these thresholds increases pooled PSO-XGBoost Accuracy from 80.28% to 81.69% and MCC from 0.6044 to 0.6348. Correct predictions increase from 57 to 58, while false positives decrease from five to four. False negatives remain at nine.

Table 5 presents selected out-of-fold predictions from Fold 4. The record at 310.452 °C has a model output of 0.5515. Increasing the threshold from 0.50 to 0.68 changes its prediction from positive to negative, matching its label. Classifications of the other displayed records remain unchanged.

Table 5. Selected out-of-fold classifications in Fold 4 at thresholds of 0.50 and 0.68.

T (°C)	Cl^- (mg/L)	O_2 (mg/L)	SCC	Output	$\tau = 0.50$	$\tau = 0.68$
300	5	0.3	1	0.039	0	0
300	100	50	1	0.995	1	1
286	0.001	38	0	0.075	0	0
310	0.03	45	0	0.551	1	0
319	0.08	328	0	0.739	1	1

Threshold adjustment changes the class decisions while retaining the continuous prediction scores; ROC-AUC therefore remains at 0.8210. Relative to the common-threshold result, the additional gain corresponds to the correction of one false positive.

5. Conclusions

Analysis of the 71-record dataset leads to the following conclusions:

(1) PSO improves XGBoost classification performance, increasing pooled four-fold Accuracy from 77.46% to 80.28%. Classification-threshold adjustment further raises Accuracy to 81.69%. The workflow achieves successive improvements through hyperparameter optimization and decision-threshold adjustment.

(2) Fixed-temperature contours characterize the model response to joint changes in chloride and oxygen concentrations. Over the same concentration domain, high-risk coverage at 340 °C exceeds that at 260 °C. This ordering remains consistent across all 25 boundary scenarios, providing quantitative evidence for comparing environmental responses between the two temperatures.

(3) Under zoning-boundary perturbations of ±0.05, spatial agreement between the raw model grids and their baseline zoning remains at least 97.57% at both temperatures. The overall zoning retains high spatial agreement, supporting the use of relative-risk regions to describe the model-response distribution within the environmental domain examined.

Author Contributions: Conceptualization, X.-Y.L., L.-W.C., X.-J.Y., Q.-H.C. and G.-H.L.; methodology, X.-Y.L., L.-W.C., X.-J.Y., Q.-H.C. and G.-H.L.; software, X.-Y.L., L.-W.C. and G.-H.L.; validation, X.-Y.L., X.-J.Y., Q.-H.C. and G.-H.L.; formal analysis, X.-Y.L., X.-J.Y. and Q.-H.C.; investigation, L.-W.C., Q.-H.C. and G.-H.L.; resources, L.-W.C., X.-J.Y., Q.-H.C. and G.-H.L.; data curation, X.-Y.L., X.-J.Y., Q.-H.C. and G.-H.L.; writing—original draft preparation, L.-W.C., X.-Y.L., Q.-H.C. and G.-H.L.; writing—review and editing, X.-Y.L., L.-W.C., X.-J.Y., Q.-H.C. and G.-H.L.; visualization, X.-Y.L., L.-W.C. and X.-J.Y.; supervision, G.-H.L.; project administration, L.-W.C., X.-J.Y., Q.-H.C. and G.-H.L.; funding acquisition, Q.-H.C. and G.-H.L. All authors have read and agreed to the published version of the manuscript.

Funding: This research was funded by the National Key Research and Development Project of China, grant number 2023YFC3008702.

Data Availability Statement: The data and code used in this study are available from the corresponding author upon reasonable request.

Conflicts of Interest: The authors declare no conflicts of interest.

References

1. Falaakh, D.F.; Bahn, C.B. Machine Learning for Modeling Intergranular Stress Corrosion Cracking of Stainless Steels in Light Water Reactors with Uncertainty Quantification and Explainability. *npj Mater. Degrad.* **2026**, *10*, 5. [CrossRef]
2. Zeng, Q.; Chen, Y.; Yang, Z.; Zhang, L.; Wang, Z.; Wang, L.; Li, J.; Wang, J. Effect of Grain Size and Grain Boundary Type on Intergranular Stress Corrosion Cracking of Austenitic Stainless Steel: A Phase-Field Study. *Corros. Sci.* **2024**, *241*, 112557. [CrossRef]
3. Andresen, P.L.; Ford, F.P. Life Prediction by Mechanistic Modeling and System Monitoring of Environmental Cracking of Iron and Nickel Alloys in Aqueous Systems. *Mater. Sci. Eng. A* **1988**, *103*, 167–184. [CrossRef]
4. Andresen, P.L.; Ford, F.P. Fundamental Modeling of Environmental Cracking for Improved Design and Lifetime Evaluation in BWRs. *Int. J. Press. Vessels Pip.* **1994**, *59*, 61–70. [CrossRef]
5. Shoji, T.; Suzuki, S.; Ballinger, R.G. Theoretical Prediction of SCC Growth Behavior–Threshold and Plateau Growth Rate. In *Proceedings of the Seventh International Symposium on Environmental Degradation of Materials in Nuclear Power Systems—Water Reactors*; NACE International: Houston, TX, USA, 1995; Volume 1, pp. 881–889.
6. Peng, Q.J.; Kwon, J.; Shoji, T. Development of a Fundamental Crack Tip Strain Rate Equation and Its Application to Quantitative Prediction of Stress Corrosion Cracking of Stainless Steels in High Temperature Oxygenated Water. *J. Nucl. Mater.* **2004**, *324*, 52–61. [CrossRef]
7. Shoji, T.; Lu, Z.; Murakami, H. Formulating Stress Corrosion Cracking Growth Rates by Combination of Crack Tip Mechanics and Crack Tip Oxidation Kinetics. *Corros. Sci.* **2010**, *52*, 769–779. [CrossRef]
8. Gao, Y.C.; Hwang, K.C. Elastic-Plastic Fields in Steady Crack Growth in a Strain-Hardening Material. In *Advances in Fracture Research: Proceedings of the 5th International Conference on Fracture*; Pergamon Press: Oxford, UK, 1982; Volume 2.
9. Macdonald, D.D.; Urquidi-Macdonald, M. A Coupled Environment Model for Stress Corrosion Cracking in Sensitized Type 304 Stainless Steel in LWR Environments. *Corros. Sci.* **1991**, *32*, 51–81. [CrossRef]
10. Macdonald, D.D.; Lu, P.-C.; Urquidi-Macdonald, M.; Yeh, T.-K. Theoretical Estimation of Crack Growth Rates in Type 304 Stainless Steel in Boiling-Water Reactor Coolant Environments. *Corrosion* **1996**, *52*, 768–785. [CrossRef]
11. Vankeerberghen, M.; Macdonald, D.D. Predicting Crack Growth Rate Vs. Temperature Behaviour of Type 304 Stainless Steel in Dilute Sulphuric Acid Solutions. *Corros. Sci.* **2002**, *44*, 1425–1441. [CrossRef]

12. Zhou, Y.; Liu, J.; Chen, K.; Shi, H.; Shang, X.; Que, Z.; Shen, Z.; Zhang, L.; Zeng, X. Predicting Intergranular Stress Corrosion Cracking of Stainless Steels in High-Temperature Water by Incorporating Crystallographic Factor. *Acta Mater.* **2025**, *297*, 121322. [CrossRef]
13. Smets, H.M.G.; Bogaerts, W.F.L. SCC Analysis of Austenitic Stainless Steels in Chloride-Bearing Water by Neural Network Techniques. *Corrosion* **1992**, *48*, 618–623. [CrossRef]
14. Smets, H.M.G.; Bogaerts, W.F.L. Deriving Corrosion Knowledge from Case Histories: The Neural Network Approach. *Mater. Des.* **1992**, *13*, 149–153. [CrossRef]
15. Smets, H.M.G.; Bogaerts, W.F.L. SCC Susceptibility Analysis of Stainless Steels in Nuclear Reactor Water: A Neural Network and Expert System Approach. *Fuzzy Sets Syst.* **1995**, *74*, 153–162. [CrossRef]
16. Lu, P.C. Using Neural Network Techniques to Predict Crack Growth Rates of Stress Corrosion. *Int. J. Mater. Prod. Technol.* **1997**, *12*, 329–345.
17. Shi, J.; Wang, J.; Macdonald, D.D. Prediction of Crack Growth Rate in Type 304 Stainless Steel Using Artificial Neural Networks and the Coupled Environment Fracture Model. *Corros. Sci.* **2014**, *89*, 69–80. [CrossRef]
18. Shi, J.; Wang, J.; Macdonald, D.D. Prediction of Primary Water Stress Corrosion Crack Growth Rates in Alloy 600 Using Artificial Neural Networks. *Corros. Sci.* **2015**, *92*, 217–227. [CrossRef]
19. Rojas Z, A.; Bakhtiari, S.; Aldrich, C.; Calo, V.M.; Iannuzzi, M. XGBoost Model for the Quantitative Assessment of Stress Corrosion Cracking. *npj Mater. Degrad.* **2024**, *8*, 126. [CrossRef]
20. Witman, M.D.; Schindler, P. MatFold: Systematic Insights into Materials Discovery Models' Performance through Standardized Cross-Validation Protocols. *Digit. Discov.* **2025**, *4*, 625–635. [CrossRef]
21. Li, K.; Rubungo, A.N.; Lei, X.; Persaud, D.; Choudhary, K.; DeCost, B.; Dieng, A.B.; Hattrick-Simpers, J. Probing out-of-Distribution Generalization in Machine Learning for Materials. *Commun. Mater.* **2025**, *6*, 9. [CrossRef]
22. Breiman, L. Bagging Predictors. *Mach. Learn.* **1996**, *24*, 123–140. [CrossRef]
23. Breiman, L. Random Forests. *Mach. Learn.* **2001**, *45*, 5–32. [CrossRef]
24. Chen, T.; Guestrin, C. Xgboost: A Scalable Tree Boosting System. In *Proceedings of the 22nd ACM SIGKDD International Conference on Knowledge Discovery and Data Mining*; Association for Computing Machinery: New York, NY, USA, 2016; pp. 785–794.
25. Kennedy, J.; Eberhart, R. Particle Swarm Optimization. In *Proceedings of ICNN'95—International Conference on Neural Networks*; IEEE: Piscataway, NJ, USA, 1995; Volume 4, pp. 1942–1948.
26. Sturrock, C.P.; Bogaerts, W.F. Empirical Learning Investigations of the Stress Corrosion Cracking of Austenitic Stainless Steels in High-Temperature Aqueous Environments. *Corrosion* **1997**, *53*, 333–343. [CrossRef]
27. Cawley, G.C.; Talbot, N.L.C. On over-Fitting in Model Selection and Subsequent Selection Bias in Performance Evaluation. *J. Mach. Learn. Res.* **2010**, *11*, 2079–2107.

Disclaimer/Publisher's Note: The statements, opinions and data contained in all publications are solely those of the individual author(s) and contributor(s) and not of MDPI and/or the editor(s). MDPI and/or the editor(s) disclaim responsibility for any injury to people or property resulting from any ideas, methods, instructions or products referred to in the content.